RSC Advances

PAPER

View Article Online
View Journal | View Issue

Cite this: *RSC Adv.*, 2026, **16**, 11077

Durable and breathable EMI shielding spacer fabrics enabled by synergistic thiol and TPU coatings

Xiujuan Wang, †[ab] Lingzhu Wang,†[b] Yuanjun Liu,*[b] Yaming Jiang*[b] and Hao Liu *[bcde]

Received 21st November 2025
Accepted 29th December 2025

DOI: 10.1039/d5ra09013j

rsc.li/rsc-advances

The proliferation of high-power electronics and 5G technology has created an increasing demand for high-performance electromagnetic interference (EMI) shielding materials that are durable, breathable, and comfortable for wearable applications. Although silver-coated textiles offer excellent shielding, their limited durability and susceptibility to corrosion hinder their practical use. This study develops a flexible, breathable, and corrosion-resistant electromagnetic interference (EMI) shielding spacer fabric using a multi-step coating strategy. The fabric features a conductive network formed by PDA-assisted electroless silver plating, followed by a thiol self-assembled layer (HDT) and finally encapsulated with a thermoplastic polyurethane (TPU) coating. The optimized composite fabric demonstrates an EMI shielding effectiveness (EMI SE) of up to 57.74 dB in the X-band, with excellent air permeability (2436.1 mm s^{-1}), superior corrosion resistance (only 7.8% resistance change after immersion in Na_2S solution), and mechanical durability (negligible resistance changes after 3000 compression cycles). Combined with its superhydrophobicity (contact angle >140°), this fabric offers a promising solution for wearable electronics and personal protective applications.

1. Introduction

The rapid proliferation of high-power electronic devices and communication systems, particularly driven by the global deployment of 5 G networks, has intensified electromagnetic interference (EMI) and electromagnetic radiation (EMR) pollution.[1,2] Such pollution not only compromises the reliable operation of sensitive electronic equipment[3] but also raises increasing concerns regarding its potential adverse effects on human health.[4] Consequently, there is a growing demand for high-performance personal protective materials capable of providing effective electromagnetic shielding.[5,6]

The detrimental effects of EMI have motivated extensive research efforts toward efficient shielding solutions.[7] Among these, electromagnetic interference shielding textiles have attracted considerable attention as a promising approach for wearable electromagnetic protection.[8] Recent review studies have systematically summarized progress in this field. For example, Akram *et al.* reviewed EMI shielding mechanisms, key performance parameters, and the fabrication of conductive textile materials based on metals, conductive polymers, and carbon-based fillers.[9] In addition, Wang *et al.* emphasized the importance of wearing comfort in EMI shielding textiles, particularly for winter-use sandwich structures, highlighting the need to balance shielding effectiveness with thermal and mechanical comfort.[10]

To meet the practical requirements of wearable applications, increasing research attention has been devoted to lightweight and flexible shielding materials. Fiber-based electromagnetic shielding materials (FESMs) are especially attractive due to their low density, intrinsic flexibility, ease of processing, and structural designability.[11,12] Textile systems can be engineered across multiple hierarchical levels, including fibers, yarns, and fabrics, and can be further functionalized through the incorporation of conductive polymers,[13] metallic coatings,[14] or conductive yarn blends,[15] thereby imparting the electrical conductivity required for effective EMI shielding.

Metals have traditionally been the dominant materials for EMI shielding owing to their high electrical conductivity. However, their application in wearable systems is often limited by high density, mechanical rigidity, and poor corrosion resistance.[16] Conductive polymer composites (CPCs) offer an alternative strategy with improved processability and design flexibility.[17] Nevertheless, achieving high electrical conductivity in CPCs generally requires high loadings of conductive fillers,

[a]*School of Arts, Hubei University of Arts and Science, Xiangyang, 441053, China. E-mail: xjwang2023@outlook.com*

[b]*School of Textile Science and Engineering, Tiangong University, Tianjin, 300387, China. E-mail: liuyuanjunsd@163.com*

[c]*Institute of Smart Wearable Electronic Textiles, Tiangong University, Tianjin, 300387, China*

[d]*Key Laboratory of Advanced Textile Composite Materials of Ministry of Education, Tiangong University, China*

[e]*State Key Laboratory of Bio-based Fiber Materials, Beijing, 100025, China. E-mail: liuhao_0760@163.com; jiangyaming@tiangong.edu.cn*

† These authors contributed equally to this work.

which can adversely affect mechanical properties such as flexibility and toughness.[18,19]

An effective approach to address these limitations involves the direct integration of conductive components onto textile substrates.[20,21] The porous and multiscale architecture of textiles provides an ideal framework for constructing interconnected conductive networks that attenuate electromagnetic waves through combined reflection and absorption mechanisms.[22] Among various surface modification techniques, electroless silver plating has been widely employed to fabricate shielding fabrics with high shielding effectiveness (SE), typically in the range of 40–80 dB.[23,24] However, the durability of metal-coated textiles remains a major challenge. Mechanical deformation, such as bending and friction, as well as exposure to corrosive environments, can readily damage the conductive layer, leading to a significant deterioration in EMI shielding performance.[25,26]

With the rapid development of wearable electronics and advanced communication technologies, including 5 G and the Internet of Things (IoT), research interest has expanded beyond EMI shielding performance alone.[27] Consequently, the development of multifunctional EMI shielding materials has emerged as an important research direction. Considerable progress has been achieved in integrating additional functionalities, such as thermal management,[28] electrothermal response,[29] flame retardancy,[30] and self-healing behavior.[31] More recently, stimuli-responsive shielding materials with tunable EMI shielding performance have been reported, enabling adaptive responses to dynamic electromagnetic environments.[32]

Several recent studies exemplify this multifunctional design strategy. Meng *et al.* fabricated a hierarchical polypyrrole nanostructure on cotton fabric followed by a PDMS coating, resulting in a lightweight and breathable textile with integrated EMI shielding, superhydrophobicity, and self-cleaning properties.[33] Zhao *et al.* employed a layer-by-layer assembly of electrospun fibers to construct multifunctional smart textiles that combine visualized thermotherapy, motion sensing, superhydrophobicity, and EMI shielding within a breathable structure.[34] Beyond textile-based systems, advanced composite architectures have also been explored. Moaref *et al.* reported an environmentally friendly sandwich-structured composite consisting of a PP/$CaCO_3$ matrix with graded concentrations of ground tire rubber (GTR) and multiwalled carbon nanotubes (MWCNTs). This design improved impedance matching and achieved an EMI SE of 55.2 dB, while simultaneously enhancing mechanical performance and reducing MWCNT consumption using recycled rubber.[35]

Recent efforts have further addressed key challenges through innovative material and structural designs. Zhang *et al.* developed a gradient structural foam-coated fabric that achieved absorption-dominated EMI shielding through impedance matching, yielding an EMI SE of 63.2 dB with low reflection and additional photothermal functionality.[36] Yang *et al.* reported a multifunctional wearable conductive nanofiber membrane exhibiting high EMI shielding efficiency, efficient Joule heating, antibacterial activity, and breathability.[37] Furthermore, Wang *et al.* demonstrated a breathable and waterproof conductive cotton fabric that integrates pressure sensing, efficient EMI shielding (>102 dB), and electrothermal performance.[38] Improvements in environmental stability have also been reported, as demonstrated by Yang *et al.*, who developed flexible polyimide/carbon nanotube composite films maintaining stable EMI shielding and Joule heating performance under harsh thermal, chemical, and mechanical conditions.[39]

Despite these advances, significant challenges remain. Achieving durable EMI shielding while maintaining mechanical robustness, wearer comfort, and multifunctional integration remains challenging for wearable applications.[40] Moreover, the integration of the intrinsic pressure-buffering capability, thermal–moisture comfort, and corrosion resistance of three-dimensional spacer fabrics with high-level and durable EMI shielding performance remains relatively underexplored.

This study aims to address this gap by developing a synergistic coating strategy to enhance the interfacial interaction and environmental stability of a conductive spacer fabric. Spacer fabric was selected as the substrate due to its excellent pressure-buffering capability, thermal-wet comfort, and favorable interfacial adhesion. By combining a thiol-based self-assembled interfacial layer with a thermoplastic polyurethane (TPU) protective coating, a flexible and corrosion-resistant conductive spacer fabric with high EMI shielding performance, breathability, and mechanical durability was successfully fabricated. This study provides a practical and scalable strategy for wearable electromagnetic protection, suitable for advanced personal protective applications.

2. Experimental section

2.1 Materials

Warp-knitted spacer fabric (SF) was purchased from Changshu Zhengfangyi Weaving Co., Ltd (China), with a thickness of 5.5 ± 0.5 mm and an area density of 300 g m^{-2}. Dopamine hydrochloride (DA, 98%), D-(+)-glucose (AR), and 1-hexadecanethiol (HDT) were sourced from Shanghai Aladdin Biochemical Technology Co., Ltd. Sodium hydroxide (NaOH), ethanol, and tris(hydroxymethyl)aminomethane (Tris, 99%) were purchased from Tianjin Comeo Chemical Reagent Co., Ltd. Silver nitrate ($AgNO_3$, 99.8%) and ammonia solution ($NH_3 \cdot H_2O$) were supplied by Tianjin Fengchuan Chemical Co., Ltd. Sodium sulfide (Na_2S) and *N*,*N*-dimethylformamide (DMF) were purchased from Tianjin Fengchuan Chemical Reagent Technology Co., Ltd. Sodium chloride (NaCl) was obtained from Tianjin Yuyuan Technology Co., Ltd. Thermoplastic Polyurethane (TPU, grade 60A) was provided from BASF, Germany. All materials and reagents were used as received, without further purification.

2.2 Fabrication process of TPU/HDT/Ag/PDA/SF composite fabric

A multifunctional TPU/HDT/Ag/PDA/SF composite fabric was fabricated through a multi-step electroless plating and dip-coating/spin-coating process. The fabrication procedure

primarily consists of five stages (as illustrated in Fig. 1): fabric pre-treatment, polydopamine surface modification, silver plating, thiol-based anti-corrosion treatment, and TPU protective coating.[41]

2.2.1 Fabrication of PDA/SF composite fabric. To enhance the stability of the modifier's bonding with the fabric, the SF was immersed in an ethanol solution and treated at room temperature for 15 min to remove residual impurities from the surface. A dopamine solution with a pH of 8.5 was prepared by dissolving 0.4325 g of tris(hydroxymethyl)aminomethane (Tris base) and 2 g of dopamine hydrochloride in 500 mL of an ethanol/water mixture ($V_{\text{Ethanol}} : V_{\text{H}_2\text{O}} = 7:3$). The cleaned SF was then immersed in the dopamine solution (with a material-to-liquid ratio of 1 : 50) and stirred at room temperature for 24 h.[42] During this period, dopamine (DA) self-polymerized into polydopamine (PDA) on the fabric surface. The treated fabric was then removed, rinsed thoroughly with deionized water, and dried at room temperature.[43]

2.2.2 Fabrication of Ag/PDA/SF composite fabric. A specific amount of silver nitrate was used to prepare aqueous silver nitrate solutions of varying concentrations (60, 80, 100, 120, and 140 g L^{-1}). First, 35.3 mL of sodium hydroxide solution (1 mol L^{-1}) was added to the solution, causing it to become turbid. Then, ammonia solution (200 mL L^{-1}) was added dropwise until the solution became clear again, yielding the desired Tollens' reagent (silver–ammonia complex solution).[44] The PDA/SF fabric was immersed in the prepared Tollens' reagent and treated in a water bath at 40 °C for 8 h. Afterwards, a glucose solution, prepared by dissolving 3.177 g of glucose in 100 mL of distilled water, was added to the mixture and allowed to react for 1 h. Finally, the fabric was removed, rinsed, dried, yielding the silver-plated spacer fabric (Ag/PDA/SF).

2.2.3 Fabrication of HDT/Ag/PDA/SF composite fabric. A 0.05 mol L^{-1} solution of 1-hexadecanethiol (HDT) was prepared using ethanol as the solvent. The dried silver-plated SF was immersed in this solution for 1 h to form a self-assembled thiol film. The fabric was then dried at 80 °C, yielding the HDT/Ag/PDA/SF composite fabric.

2.2.4 Fabrication of TPU/HDT/Ag/PDA/SF composite fabric. TPU pellets were mixed with *N*,*N*-dimethylformamide (DMF) solution in a sealed conical flask according to a predetermined mass fraction. The mixture was stirred at 60 °C for 4 h, resulting in a transparent and homogeneous TPU solution. The SF was immersed in the TPU solution for 5 min, removed, and then placed in a centrifuge for 3 min at 600 rpm. Subsequently, it was dried in a vacuum oven at 80 °C for 5 min. After repeating this centrifugation/drying cycle twice, the SF was vacuum-dried at 80 °C for 2 h, ultimately yielding the TPU/HDT/Ag/PDA/SF composite fabric.

2.3 Coating characterization

The surface morphology of the conductive composite fabrics was observed using a Regulus 8100 cold field emission scanning electron microscope (SEM, Hitachi). Elemental composition

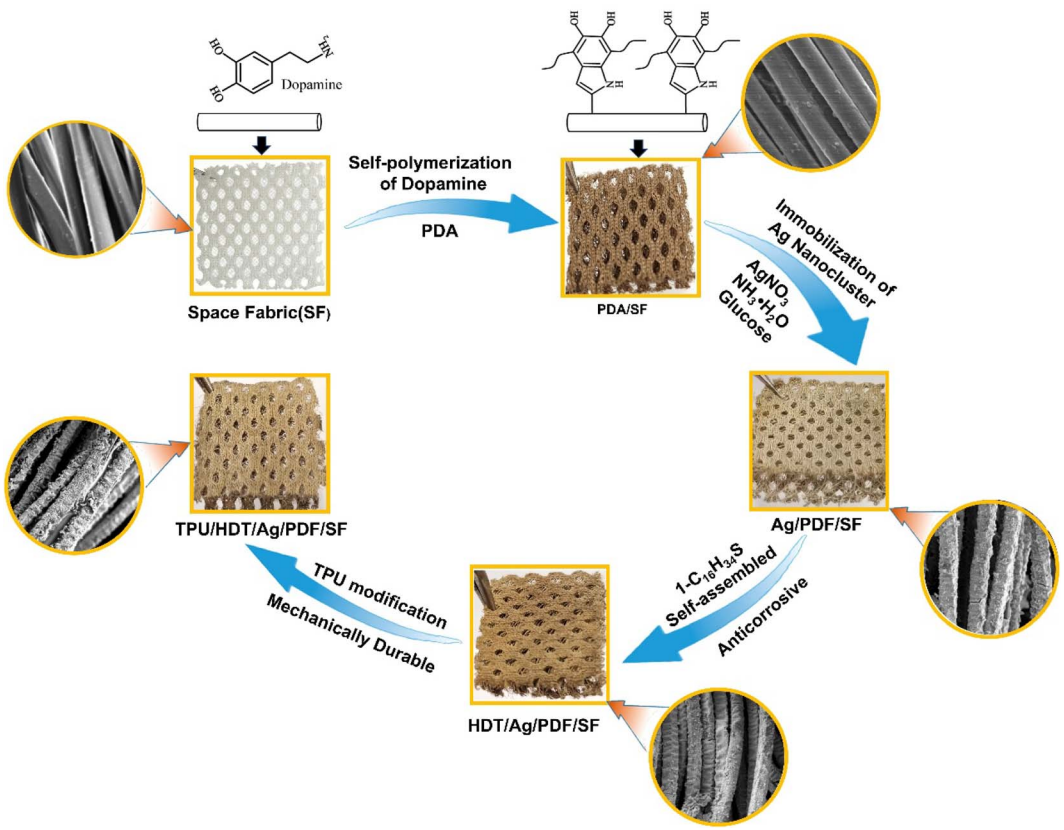

Fig. 1 Schematic diagram illustrating the fabrication process of the TPU/HDT/Ag/PDA/SF conductive composite spacer fabric.

and distribution data on the sample surface were obtained using an OXFORD energy dispersive X-ray spectrometer (EDS). Fourier transform infrared (FTIR) spectra of the SF, PDA/SF, Ag/PDA/SF, HDT/Ag/PDA/SF, and TPU/HDT/Ag/PDA/SF fabrics were recorded using a Nicolet iS10 FTIR spectrometer (Thermo Fisher Scientific), with a scanning frequency range of 4000–400 cm^{-1}. The crystal structure of the Ag particles was identified using an X-ray diffractometer (XRD, BRUKER). The weight percentage of silver particles in the Ag/PDA/SF composite was determined using a TG209F thermogravimetric analyzer (NETZSCH, Germany).

2.4 Electrical conductivity test

The electrical conductivity of the composite fabrics was measured using a U3402A multimeter (Agilent Technologies). The composite fabric was placed between two copper sheets, with a 20 g weight placed on the top copper sheet. Wires were soldered to the copper sheets to connect the electrodes to the Agilent multimeter, and the resistance of the composite fabric was recorded.

2.5 Electrochemical performance test

Electrochemical performance tests were conducted using a CHI660E electrochemical workstation (Shanghai Chenhua Instrument Co., Ltd). A three-electrode system was employed, with the composite fabric as the working electrode, a platinum electrode as the counter electrode, and a saturated calomel electrode (SCE) as the reference electrode. The test temperature was maintained at (25 ± 1) °C. Cyclic voltammetry (CV) curves were measured within a potential range of −1.5 to 1 V at a scan rate of 100 mV s^{-1}. Potentiodynamic polarization curves were measured within a potential range of −1.5 to 1 V at a scan rate of 10 mV s^{-1}. Electrochemical impedance spectroscopy (EIS) was performed over a frequency range of 1 to 10^5 Hz with an amplitude of 5 mV. The medium for CV tests was a 0.1 mol L^{-1} NaOH solution, while the medium for both polarization curve and EIS measurements was a 0.05 mol L^{-1} NaCl solution.

2.6 Electromagnetic shielding performance test

The electromagnetic shielding performance of the samples in the X-band was tested using an Agilent E5071C vector network analyzer (USA) *via* the waveguide method. The sample size was 24 × 22 × 6 mm. The test frequency range was 8.2–12.4 GHz. The shielding effectiveness (SE) of the Ag/PDA/SF, HDT/Ag/PDA/SF, and TPU/HDT/Ag/PDA/SF fabrics was measured.

2.7 Air permeability and hydrophobicity tests

The air permeability of the Ag/PDA/SF composite fabric and pure cotton fabric was measured using a fully automatic air permeability tester (YH461h, Ningbo Textile Instrument Co., Ltd, Ningbo, China). The contact angle of the fabrics was measured using a JC2000DM contact angle tester (Shanghai Zhongchen Digital Technology Equipment Co., Ltd). The reported contact angle is the average of five measurements taken at different locations on the material surface.

2.8 Softness and stability tests

Fabric softness was evaluated by testing the relationship between displacement and load using a TP-550 fabric mechanics tester (Tianjin Zhirou Technology Co., Ltd). The load magnitude indirectly reflects the fabric softness. Compression displacements were set to 10, 20, 30, 40, and 50% of the fabric thickness, with a compression speed of 0.1 mm s^{-1}. The load change from the balance was recorded and converted into pressure for easier comparison, reflecting the fabric softness. For the same compression displacement, a higher pressure indicates a stiffer fabric, and *vice versa*.

For fabric stability testing, cyclic compression tests were performed using the TP-550 tension/compression tester. The compression displacement was set to 3 mm, and the compression speed was 0.3 mm s^{-1}, for 3000 cycles. The electrical signal of the fabric was collected to determine the degree of resistance change.

For washing stability testing, a washing experiment was designed with reference to the relevant procedures of GB/T 8629–2017. A beaker was used to simulate the washing machine environment, and a magnetic stirrer provided the agitation force, set to 500 rpm. The Ag/PDA/SF, HDT/Ag/PDA/SF, and TPU/HDT/Ag/PDA/SF fabrics were placed in separate beakers for washing. They were removed every 30 min, dried in a constant temperature blast drying oven at 60 °C, and then weighed and tested for resistance. The resistance and weight after each washing cycle were recorded.

3. Results and discussion

3.1 Characterization of spacer fabric coatings

The surface morphology and structure of the five composite fabrics—SF, PDA/SF, Ag/PDA/SF, HDT/Ag/PDA/SF, and TPU/HDT/Ag/PDA/SF—were characterized using scanning electron microscopy (SEM) (Fig. 2).

As depicted in Fig. 2a, the surface of the pristine SF fabric is smooth, with a small number of impurities on and between the fibers. In contrast, the surface of the silver-plated fibers becomes notably rougher, displaying a distinct granular Ag layer deposited on the fiber surface (Fig. 2b). To enhance chemical reactivity of the fiber surface, polydopamine (PDA) was adsorbed onto the fibers *via* the self-polymerization of dopamine under alkaline conditions. The interaction between Ag^+ ions and the catechol groups, primarily through chelation, facilitated the migration of Ag precursors onto the PDA layer. The amount of adsorbed Ag^+ ultimately depended on the concentration of $AgNO_3$. After reduction by glucose, the Ag^+ ions were fully converted into Ag particles that coated the fibers. These interconnected micron-sized particles form a conductive network within the fabric.

Oxidation and corrosion of metallic materials remain significant challenges. Encapsulating the Ag particles with 1-hexadecanethiol (HDT) can effectively mitigate the corrosion issues.[2,37] Following immersion in the HDT solution for 1 h, a self-assembled thiol film formed on the fabric surface, resulting in wrinkles and a less granular appearance (Fig. 2c).

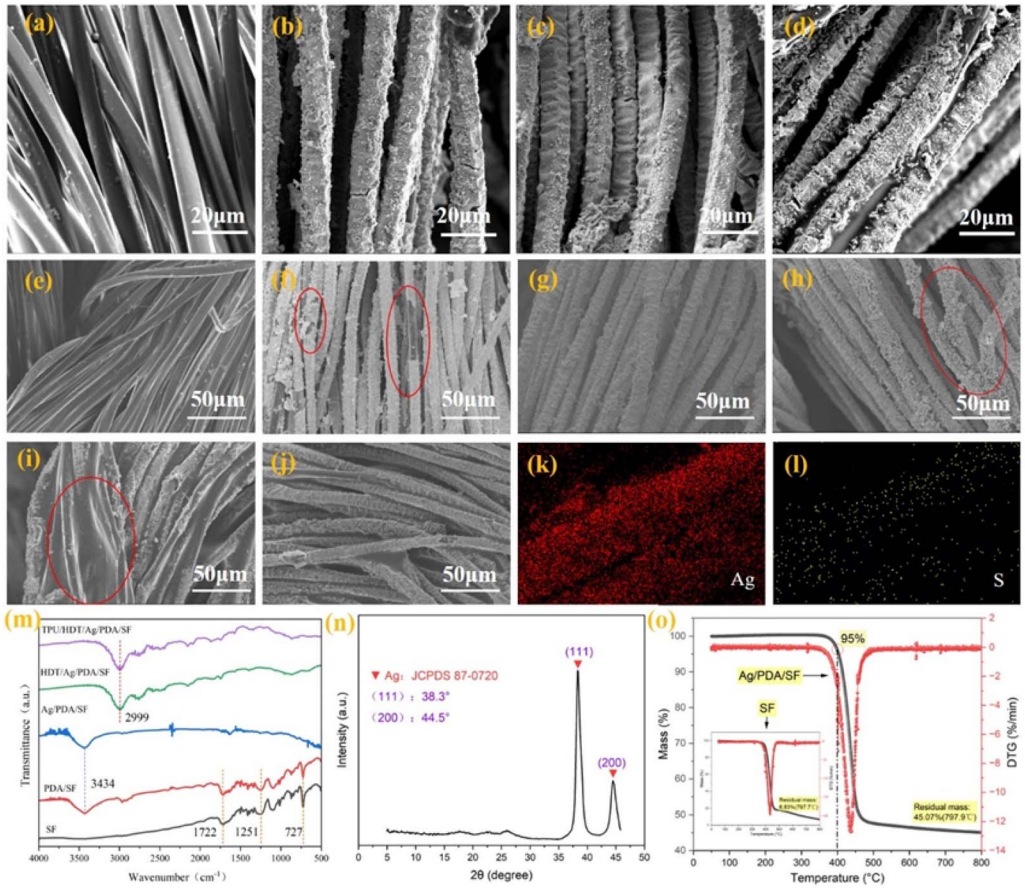

Fig. 2 SEM images of spacer fabrics with different surface modifications: (a) pristine spacer fabric (SF); (b) Ag/PDA/SF; (c) HDT/Ag/PDA/SF; and (d) TPU/HDT/Ag/PDA/SF. SEM images of silver-plated spacer fabrics prepared with different $AgNO_3$ concentrations: (e) pristine SF, (f) 60 g L^{-1}, (g) 80 g L^{-1}, and (h) 100 g L^{-1}. SEM images of TPU/HDT/Ag/PDA/SF treated at an $AgNO_3$ concentration of 80 g L^{-1} with a TPU immersion time of 5 min and different centrifugation times: (i) 1 min and (j) 3 min. (k) EDS elemental mapping of Ag on the fabric surface. (l) EDS elemental mapping of S on the fabric surface after thiol coating. (m) FTIR spectra of the composite fabrics. (n) XRD patterns of TPU/HDT/Ag/PDA/SF. (o) TG curves of the fabrics before and after silver plating.

Although the introduction of PDA between the Ag particles and the fibers enhanced their interfacial adhesion, the silver particles were still susceptible to detachment under external force, leading to decreased conductivity and consequently reduced electromagnetic shielding performance. To further improve the interfacial adhesion between the Ag particles and between the particles and the fabric, the conductive fabric was immersed in a TPU solution. A centrifuge was used to aid the diffusion of TPU into the fabric. After curing, TPU acted as an adhesive layer, firmly binding the Ag particles to the fibers, thus significantly enhancing the stability of the composite fabric, allowing it to retain its performance under external stress. As shown in Fig. 2d, TPU tightly adhered the silver particles to the fabric surface, improving the interfacial adhesion of the fibers. The concentration of silver nitrate influenced the thickness of the silver layer on the fabric surface. In this study, samples were prepared using silver nitrate concentrations of 80, 100, and 120 g L^{-1}, with a fixed dopamine concentration of 4 g L^{-1}. Fig. 2a–f show that as the silver nitrate concentration increased, the silver layer on the fabric surface became denser, and the gaps between the silver particles narrowed. When the silver nitrate concentration reached 100 g L^{-1}, a dense and continuous silver layer formed on the fabric surface (Fig. 2g), contributing to the enhanced electrical conductivity and EMI SE. A further increase in the silver nitrate concentration led to the formation of numerous silver particle aggregates on the fabric surface (Fig. 2h), which adversely affected the appearance and stability of the conductive composite fabric.

Fig. 2 i–j show SEM images of TPU/HDT/Ag/PDA/SF. The TPU coating strengthened the binding between the silver particles and the fibers, causing the Ag particles to adhere more closely to the fiber surface. The TPU content on the fabric surface was influenced by the centrifugation time. At a centrifugation time of 1 minute, TPU formed large-area agglomerates on the fabric surface (Fig. 2i), which impaired both air permeability and electrical conductivity. With a centrifugation time of 2 minutes, the TPU layer became thinner. At 3 minutes, the interfaces between the Ag particles were defined (Fig. 2j), and a minimal amount of TPU adhered to the fiber surface, thereby improving the interfacial adhesion of the composite fabric.

Fig. 2k–l illustrate the elemental compositions and proportions on the surfaces of the Ag/PDA/SF, HDT/Ag/PDA/SF fabrics. The results reveal that, following silver plating, the composite fabric surface is uniformly coated with silver, with a content exceeding 85%, demonstrating that silver particles evenly distributed and completely cover the fabric surface. Subsequent thiol treatment results in the presence of sulfur (S) on the fabric surface, confirming the successful self-assembly of thiol onto the fabric. Moreover, the elemental distribution is homogeneously spread throughout the matrix, indicating a well-integrated and uniform modification.

Fig. 2m presents the FTIR spectra of SF, PDA/SF, Ag/PDA/SF, HDT/Ag/PDA/SF, and TPU/HDT/Ag/PDA/SF. The chemical interactions between PDA and HDT were confirmed by FTIR analysis. The SF spectrum exhibits characteristic absorption peaks at approximately 1722 cm^{-1}, 1251 cm^{-1}, and 727 cm^{-1}, among others. The peak at 1722 cm^{-1} corresponds to C═O stretching vibrations, the peak at 1251 cm^{-1} corresponds to the C–O stretching, and the peak at 727 cm^{-1} is attributed to the in-plane rocking vibration of $-CH_2$ on *para*-disubstituted benzene rings, consistent with the standard polyester spectrum. The PDA/SF spectrum shows a peak at 3434 cm^{-1}, corresponding to O–H groups, confirming the polymerization of dopamine on the fabric. The HDT/Ag/PDA/SF spectrum exhibits a peak at 2999 cm^{-1}, corresponding to the S–H stretching vibration region, which confirms the self-assembly of 1-hexadecanethiol on the fabric surface.

Fig. 2n shows the XRD analysis of the TPU/HDT/Ag/PDA/SF fabric. Comparing the test results with the standard JCPDS patterns reveals distinct crystal plane diffraction peaks corresponding to the (111) and (200) planes of Ag at 2θ values of 38.3° and 44.5°, respectively.

The peaks are sharp and narrow, with no significant secondary phases observed, indicating high purity and crystallinity of the silver grains. The modification with HDT and TPU does not alter the crystal structure of the Ag particles.

Fig. 2o shows the thermogravimetric (TG) analysis of the fabric before and after silver plating. After thermal degradation at 800 °C in a nitrogen atmosphere, the residual mass percentages of SF and Ag/PDA/SF are approximately 6.8% and 45.1%, respectively, which allows for the determination of the silver content in the Ag/PDA/SF composite fabric.

3.2. Electromagnetic shielding performance of silver-plated SF

Fig. 3 presents the electromagnetic shielding effectiveness (EMI SE) of SF prepared with varying silver nitrate concentrations, as well as those with different coatings.

As illustrated in Fig. 3a, the reflection loss (SE_R) of the Ag/PDA/SF fabric initially increases and then decreases as the silver nitrate concentration rises. The absorption loss (SE_A) is lowest at a concentration of 60 g L^{-1} and remains nearly constant (with a deviation of less than 10%) between 80–140 g L^{-1}. The total shielding effectiveness (SE_T) reaches its maximum value of 57.74 dB at 80 g L^{-1}. Fig. 3b shows the EMI SE across the 8.2–12.4 GHz frequency range, revealing that for concentrations between 80–140 g L^{-1}, the EMI SE fluctuates within a certain range, with the 80 g L^{-1} sample peaking at 10.2 GHz. From Fig. 3a and b, it can be observed that as the silver nitrate concentration increases, the EMI SE of the fabric rises initially. However, once the concentration reaches 80 g L^{-1}, the EMI SE peaks and then stabilizes. As shown in Fig. 3c, the shielding effectiveness components of Ag/PDA/SF spacer fabrics prepared at different silver nitrate concentrations. For all samples, the absorption loss (SEA) is significantly higher than the reflection loss (SER), indicating an absorption-dominated EMI shielding mechanism. At a silver nitrate concentration of 60 g L^{-1}, the total shielding effectiveness (SE_T) is 37.92 dB, with SE_A and SE_R values of 26.41 and 11.51 dB, respectively, corresponding to an SE_A contribution of 69.6%. Upon increasing the silver nitrate concentration to 80, 100, and 120 g L^{-1}, the SET increases to 57.74, 54.07, and 54.83 dB, respectively, while SEA dominates the shielding performance with values of 45.35, 44.49, and 48.39 dB. In all cases, the contribution of SEA exceeds 75%, reaching a maximum of 88.3% at 120 g L^{-1}, confirming the dominant role of absorption in electromagnetic wave attenuation. This behavior is attributed to the formation of hierarchical heterogeneous interfaces and interconnected conductive networks within the Ag/PDA/SF structure. The PDA interlayer enhances interfacial adhesion and introduces additional dielectric loss, which synergistically couples with the conductive loss of the silver network. Increasing silver deposition results in a more continuous conductive pathway, promoting multiple internal reflections, scattering, and polarization relaxation, thereby enhancing energy dissipation. Meanwhile, the moderate electrical conductivity and structural gradient improve impedance matching with free space, suppressing excessive surface reflection and maintaining low SER values. These results demonstrate that regulating the silver nitrate concentration effectively optimizes the conductive architecture and interfacial characteristics of Ag/PDA/SF fabrics, enabling efficient absorption-dominated EMI shielding suitable for lightweight and flexible textile-based applications.

The total EMI shielding effectiveness (SE_T) of a material can be expressed by the following equation:

$$SE_T(dB) = SE_R + SE_A + SE_M \quad (1)$$

where SE_R, SE_A, SE_M represent the reflection loss, absorption loss, and multiple reflection loss, respectively, during the shielding process. Furthermore, in transmission line theory, SE_M is closely related to SE_A. When $SE_A > 15$ dB, the multiple reflection loss (SE_M) can generally be neglected.

The electromagnetic shielding mechanism is typically analyzed using the absorption (A), reflection (R), and transmission (T) coefficients, which correspond to the proportions of incident wave power absorbed, reflected, and transmitted by the shielding material, respectively. These parameters can be calculated from the scattering parameters (S_{11} and S_{21}) measured by a vector network analyzer. The relationships are given by:

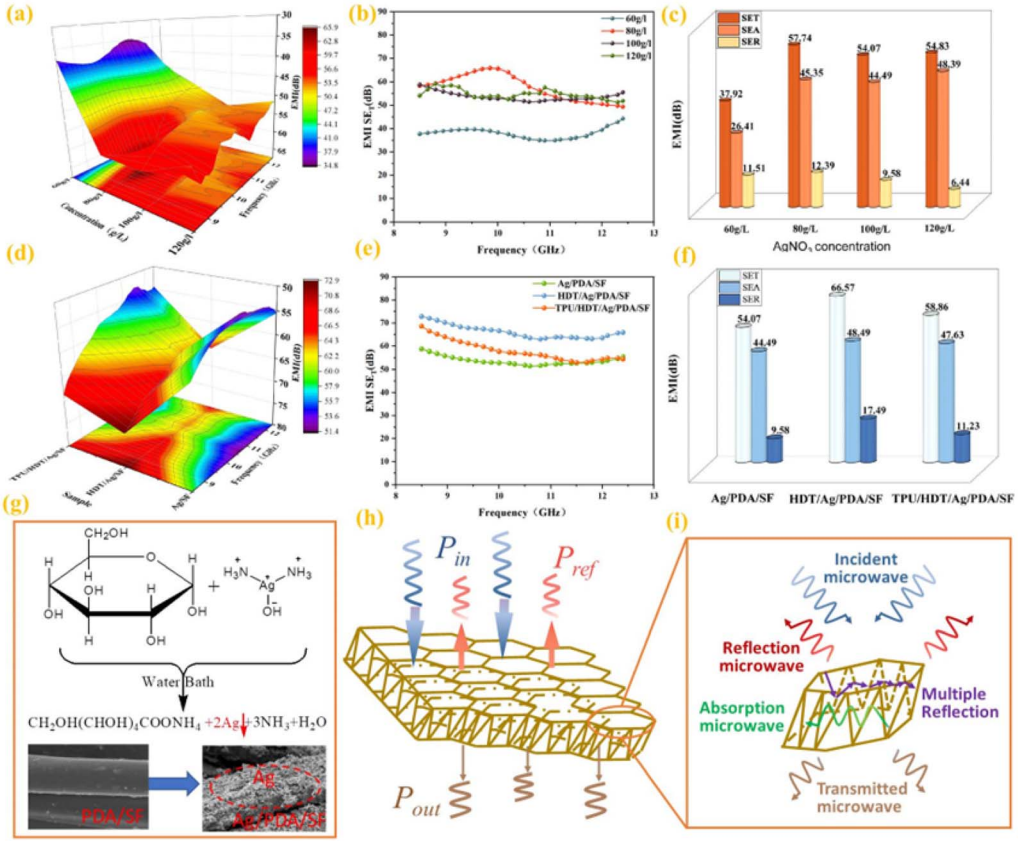

Fig. 3 Electromagnetic shielding performance and shielding mechanism of Ag/PDA/SF silver-plated spacer fabrics. (a) Three-dimensional contour maps of electromagnetic shielding effectiveness (SE) for Ag/PDA/SF samples prepared with different silver nitrate concentrations in the 8–12 GHz frequency range. (b) Frequency-dependent SE curves of the corresponding samples. (c) Average total shielding effectiveness (SE_T), absorption loss (SE_A), and reflection loss (SE_R) for each sample in the 8–12 GHz band. (d–f) Comparison of shielding performance of three functionalized samples (Ag/PDA/SF, HDT/Ag/PDA/SF, and TPU/HDT/Ag/PDA/SF) at a silver nitrate concentration of 80 g L^{-1} in the 8–12 GHz band: (d) three-dimensional SE contour maps; (e) SE as a function of frequency; (f) average values of SE_T, SE_A, and SE_R. (g) Schematic illustration of the chemical modification process of the silver-plated spacer fabric. (h) Conceptual model of electromagnetic power dissipation during shielding, including reflection loss (P_{ref}), absorption loss (P_{in}), and transmission (P_{out}). (i) Attenuation mechanisms of incident microwaves in shielding materials, including reflection, absorption, and multiple internal reflections.

$$R = |S_{11}|^2 \quad (2)$$

$$T = |S_{21}|^2 \quad (3)$$

$$A + R + T = 1 \quad (4)$$

Furthermore, the values of SE_T, SE_R and SE_A can be further calculated from these electromagnetic parameters as follows:

$$SE_T(dB) = -10 \log T \quad (5)$$

$$SE_R(dB) = -10 \log(1 - R) \quad (6)$$

$$SE_A(dB) = SE_T - SE_R \quad (7)$$

Here, SE_T, SE_R, SE_A represent the total, reflection, and absorption EMI shielding effectiveness, respectively.

As shown in Fig. 3d–f, all three spacer fabrics exhibit continuous and stable EMI shielding responses throughout the X-band (8–12 GHz), indicating that the silver-based conductive networks formed within the three-dimensional spacer structures are effective over the entire frequency range. The three-dimensional distribution maps in Fig. 3d clearly reveal distinct shielding levels among the samples: Ag/PDA/SF displays the lowest EMI shielding intensity, whereas a pronounced enhancement is observed after HDT modification. Upon further TPU encapsulation, the maximum shielding level slightly decreases, but the overall distribution becomes more uniform, suggesting improved broadband stability. The corresponding frequency-dependent SE_T curves in Fig. 3e quantitatively confirm this trend, with Ag/PDA/SF exhibiting SE_T values of approximately 52–58 dB, HDT/Ag/PDA/SF achieving significantly higher values of about 63–72 dB, and TPU/HDT/Ag/PDA/SF maintaining a high SE_T of approximately 55–67 dB, which remains consistently superior to that of the unmodified fabric.

Further insight into the shielding mechanisms is provided by the quantitative decomposition shown in Fig. 3f. For all samples, absorption loss (SE_A) contributes dominantly to the total shielding effectiveness, far exceeding the reflection loss (SE_R), which is characteristic of porous three-dimensional

architectures that promote multiple internal reflections and electromagnetic energy dissipation. Compared with Ag/PDA/SF ($SE_T = 54.07$ dB, $SE_A = 44.49$ dB, $SE_R = 9.58$ dB), HDT modification markedly increases SE_T to 66.57 dB, accompanied by simultaneous enhancements in both SE_A and SE_R. This improvement can be attributed to the thiol-based HDT layer, which strengthens interfacial bonding between silver particles and the fiber substrate, enhances electrical continuity, and improves impedance matching, thereby reinforcing conductive loss and interfacial reflection. After TPU coating, the SE_T slightly decreases to 58.86 dB; however, SE_A remains high at 47.63 dB, while SE_R is maintained at a relatively low level (11.23 dB). Although the electrically insulating TPU layer partially suppresses surface reflection, it introduces additional heterogeneous interfaces and prolongs electromagnetic wave propagation pathways within the spacer fabric, thereby intensifying polarization loss and multiple scattering. Overall, the synergistic regulation achieved by HDT and TPU balances high absorption-dominated shielding, low reflection leakage, and broadband stability, accounting for the performance differences observed in Fig. 3d–e and highlighting the TPU/HDT/Ag/PDA/SF fabric as a promising candidate for advanced wearable and protective EMI shielding applications.

As illustrated in Fig. 3g–i, the schematic diagram provides a systematic interpretation of the EMI shielding mechanism of the Ag-based spacer fabrics from the perspectives of structural evolution and energy transmission. Fig. 3g indicate that, after PDA pretreatment, silver particles are uniformly deposited on the fiber surface to form a continuous coating (Ag/PDA/SF), which serves as stable conductive pathways for electromagnetic shielding. Fig. 3h show that, when an incident electromagnetic wave with power P_{in} impinges on the three-dimensional spacer fabric, a portion of the energy is initially reflected (P_{ref}) due to impedance mismatch between the conductive surface layer and air. The remaining electromagnetic waves penetrate the interior of the fabric, where the conductive framework formed by the silver coating induces free charge carrier motion and converts electromagnetic energy into Joule heat, thereby significantly reducing the transmitted power (P_{out}).

Meanwhile, the unique three-dimensional porous architecture of the spacer fabric promotes multiple scattering and internal reflections of electromagnetic waves at the interfaces between the fibrous skeleton and the pores, effectively prolonging the propagation pathways and enhancing energy dissipation. The enlarged schematic Fig. 3i further demonstrates the synergistic contributions of reflection, absorption, and multiple internal reflection within the structure, with absorption playing the dominant role. This qualitative mechanism is fully consistent with the quantitative results in Fig. 3f, where SE_A is significantly higher than SE_R. Overall, Fig. 3g–i visually elucidates a cooperative EMI shielding mechanism involving surface reflection, bulk absorption, and multiple internal reflections, directly correlating the structural characteristics of the spacer fabric with its macroscopic shielding performance.

3.3 Electrochemical performance of silver-plated spacer fabric

Fig. 4 illustrates the changes in surface morphology and resistance over time for Ag/PDA/SF, HDT/Ag/PDA/SF, and TPU/HDT/Ag/PDA/SF composite fabrics immersed in a 0.1% Na_2S solution.

As shown in Fig. 4a, after corrosion in the Na_2S solution, both the Ag/PDA/SF and TPU/Ag/PDA/SF fabrics exhibit significant discoloration, which intensifies with prolonged immersion. This discoloration is attributed to the reaction between Na_2S and silver, resulting in the formation of blackish-brown Ag_2S on the surface of the silver coating. In contrast, the HDT/Ag/PDA/SF and TPU/HDT/Ag/PDA/SF fabrics display no notable discoloration, suggesting superior corrosion resistance provided by the HDT self-assembled film. The HDT forms a dense self-assembled layer on the silver coating surface, effectively isolating the silver particles from direct contact with the Na_2S solution. In comparison, TPU coating alone does not sufficiently isolate the silver layer from Na_2S, failing to provide effective corrosion protection.

As shown in Fig. 4b, with prolonged exposure to the Na_2S solution, the resistance of the Ag/PDA/SF and TPU/Ag/PDA/SF fabrics increases gradually, followed by a sharp rise after 30 minutes, with resistance changes of 1104% and 433%, respectively. In contrast, the resistance changes for the HDT/Ag/PDA/SF and TPU/HDT/Ag/PDA/SF fabrics are much lower, at 7.8% and 36.7%, respectively. Moreover, the resistance of these fabrics remains nearly constant as the corrosion time increases, indicating that the 1-hexadecanethiol self-assembled film effectively protects the silver layer from corrosion, demonstrating excellent anti-corrosion performance.

Fig. 4c–e compare the electrochemical performance of HDT/Ag/PDA/SF and Ag/PDA/SF fabrics. Fig. 4c shows that the cyclic voltammetry (CV) curve of Ag/PDA/SF exhibits distinct oxidation and reduction peaks. In contrast, the CV curve of HDT/Ag/PDA/SF is nearly a straight line, with no observable oxidation or reduction peaks, indicating a significant reduction in both peak currents. This suggests that the 1-hexadecanethiol self-assembled film effectively inhibits the oxidation process. The polarization curves in Fig. 4d further demonstrate that the 1-hexadecanethiol self-assembled film significantly inhibits the corrosion of the silver coating, as both the cathodic and anodic current densities are markedly reduced. These results indicate that the self-assembled film suppresses both anodic and cathodic reaction processes. The polarization curves were fitted, and the inhibition efficiency (η) was calculated according to eqn (8) to evaluate the corrosion inhibition effect of the self-assembled film. The calculation reveals that after protection with 1-hexadecanethiol, the corrosion current density decreased from 23.64 $\mu A \cdot cm^{-2}$ to 3.17 $\mu A \cdot cm^{-2}$, yielding an inhibition efficiency of 86.60%.

$$\eta = \frac{J_{0,corr} - J_{corr}}{J_{0,corr}} \times 100\% \quad (8)$$

where: $J_{0,corr}$ and J_{corr} represent the self-corrosion current densities measured in the Na_2S solution for the silver coating

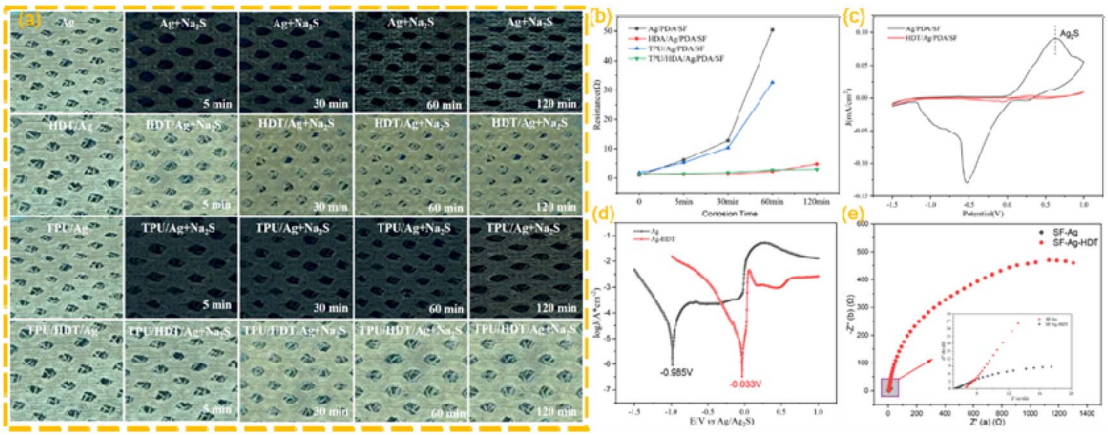

Fig. 4 (a) Appearance and (b) resistance-time curves of the four samples immersed in Na_2S solution over time. (c) CV curves, (d) Tafel plots, (e) Nyquist plots.

without and with the self-assembled film, respectively (Table 1).

As shown in the impedance spectra in Fig. 4e, the Ag/PDA/SF fabric exhibits a semicircular arc in the high-frequency region of the corrosion medium, while the impedance spectrum of the HDT/Ag/PDA/SF fabric with the 1-hexadecanethiol protective coating shows a larger semicircle in the high-frequency range. This behavior is attributed to the self-assembled film, which effectively suppresses the electrochemical corrosion reaction at the interface between the silver electrode and the solution. The larger radius of the semicircle indicates a higher resistance to charge transfer, suggesting enhanced corrosion protection provided by the self-assembled film.

The corrosion inhibition effect of HDT can be further understood from the perspective of charge carrier transfer at the metal–electrolyte interface. The thiol group (–SH) in HDT exhibits a strong chemical affinity toward silver, forming stable Ag–S bonds and generating a densely packed self-assembled monolayer on the Ag surface. This organic layer acts as an effective physical and electronic barrier, which blocks direct contact between the silver surface and corrosive ions in the electrolyte.

More importantly, the HDT self-assembled layer significantly suppresses interfacial charge transfer by increasing the electron tunneling resistance between the silver surface and the surrounding electrolyte. As a result, both anodic dissolution of Ag and cathodic reduction reactions is effectively inhibited, leading to reduced corrosion current density and enhanced charge transfer resistance, as evidenced by the CV, Tafel, and EIS results. Therefore, the "carrier-transfer inhibition" refers to the restricted migration of charge carriers across the Ag/electrolyte interface induced by the compact HDT molecular layer, rather than bulk conductivity degradation within the Ag network.

Table 1 Corrosion resistance test parameters

Samples	E_{corr}/mV	J_{corr}/(μA cm^{-2})	η/%
Ag	−0.987	23.64	—
Ag-HDT	−0.031	3.168	86.60

3.4 Wearable performance of silver-plated SF

Air permeability, a key factor in evaluating wearing comfort, is defined as the ability of gas molecules to pass through a fabric. While pure cotton fabric exhibits an air permeability of 585.3 mm s^{-1}, recent advancements in breathable composite materials have led to the development of various conductive textiles, such as reduced graphene oxide (RGO)/MXene-integrated cotton (RMC),[45] $Ti_3C_2T_3$-coated cotton (M-CF),[46] PEDOT:PSS-modified 3D spacer fabric for e-skin sensing (PPSF),[40] and screen-printed CNT textiles (CNTs-CF).[47] Although these materials demonstrate reasonable breathability, the silver-plated spacer fabric developed in this study exhibits an exceptional air permeability of 2436.1 mm s^{-1}, which is approximately 4.2 to 27.6 times higher than that of the referenced materials (Fig. 5a). This remarkable performance highlights the potential of our fabric as a highly breathable EMI shielding material, significantly enhancing wearer comfort.

The surface wettability of the fabrics was assessed through contact angle measurements (Fig. 5b). The pristine SF exhibited a contact angle of 58.38°, indicating its hydrophilic nature. In contrast, after modification with 1-hexadecanethiol (HDT), the contact angle increased substantially to 142.49°, imparting superhydrophobicity. This transition is attributed to the synergistic effect of the micro-scale roughness induced by silver particles and the low surface energy provided by the HDT layer. The resulting HDT/Ag/PDA/SF fabric, with a contact angle exceeding 140°, exhibits excellent waterproofing, ensuring operational reliability even under harsh conditions such as rain or salt spray.

Visual inspection after 10 manual pressing cycles (Fig. 5c) revealed that the TPU/HDT/Ag/PDA/SF fabric exhibited no visible shedding of silver particles, whereas the other fabric variants showed varying degrees of particle detachment. These findings highlight the protective role of the TPU coating and

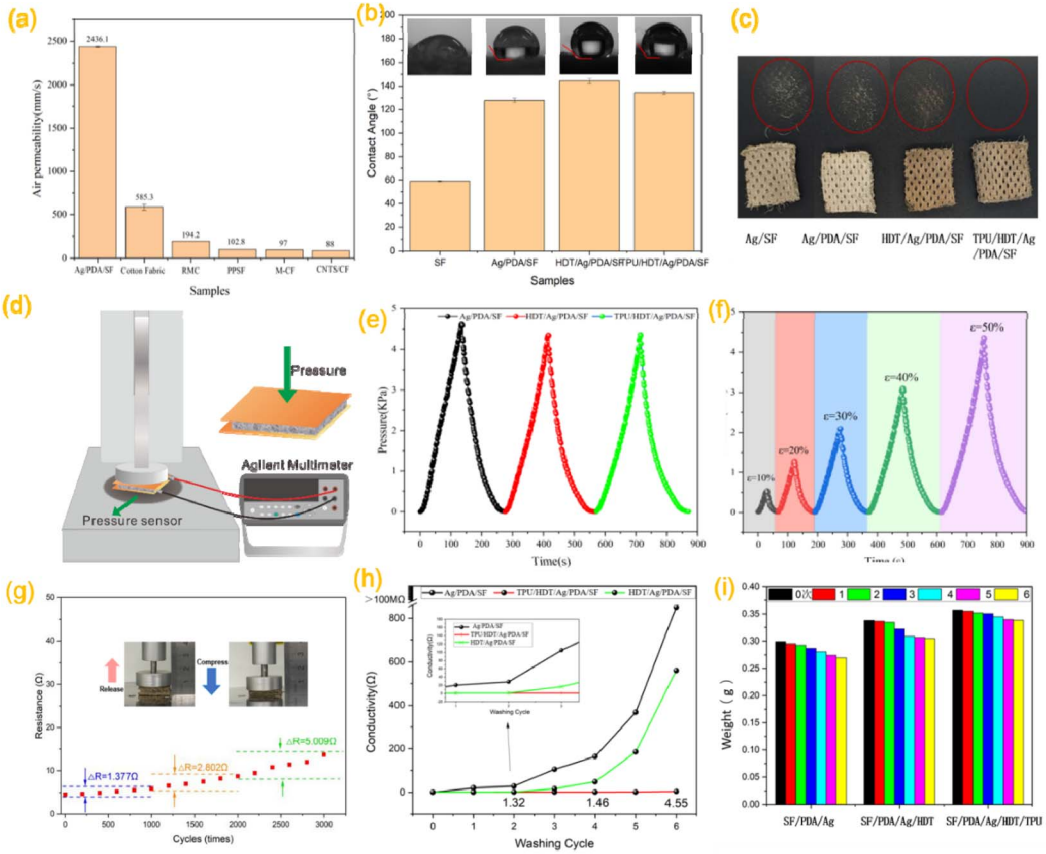

Fig. 5 (a) Air permeability and (b) water contact angle of SF, Ag/PDA/SF, HDT/Ag/PDA/SF, and TPU/HDT/Ag/PDA/SF fabrics; (c) powder shedding after 10 presses for different fabrics. (d) Schematic diagram of the sample test principle, (e) load values at 50% strain for different fabrics, (f) load values for TPU/HDT/Ag/PDA/SF fabric at different compression levels. (g) Cyclic compression stability of the spacer fabrics. (h) Electrical resistance variation and (i) weight change of the fabrics after repeated washing cycles.

demonstrate the superior stability of the TPU/HDT/Ag/PDA/SF fabric under cyclic mechanical stress, in comparison to the other three fabrics.

Softness was evaluated by measuring the pressure–displacement relationship during compression tests (schematic in Fig. 5d). As shown in Fig. 5e, the load values at 50% strain reveal that both thiol immersion and TPU coating improved fabric softness, with recorded pressures of 4.35 kPa and 4.36 kPa, respectively. This improvement can be attributed to the partial removal of loosely bound silver particles during the thiol reaction, followed by the centrifugal spinning process of TPU, which together contributed to a reduction in the overall stiffness of the composite fabric. Additionally, the load values for the TPU/HDT/Ag/PDA/SF fabric at different compression levels (Fig. 5f) demonstrate a progressive increase in pressure with strain, indicating a corresponding rise in fabric hardness.

The electrical stability of the TPU/HDT/Ag/PDA/SF fabric under cyclic compression is illustrated in Fig. 5g. After 1000, 2000, and 3000 compression cycles, the resistance increased by only 1.377 Ω, 2.802 Ω, and 5.009 Ω, respectively, demonstrating exceptional mechanical durability. Washing stability was assessed following the procedures outlined in GB/T 8629-2017. As shown in Fig. 5h, the Ag/PDA/SF fabric exhibited a significant increase in resistance after the second wash, while the HDT/Ag/PDA/SF fabric experienced notable degradation after the fourth wash (120 min). By the sixth wash, the Ag/PDA/SF fabric failed electrically. In contrast, the TPU/HDT/Ag/PDA/SF fabric maintained stable conductivity, with a minimal resistance change of 4.3 Ω after six washing cycles. The corresponding mass loss trends (Fig. 5i) confirmed that the TPU encapsulation effectively mitigated the detachment of the conductive material, preserving the integrity of the conductive network during repeated laundering.

4. Conclusion

In this study, we have successfully developed a flexible, breathable, and multifunctional TPU/HDT/Ag/PDA/SF composite fabric for high-performance EMI shielding using a simple yet effective synergistic coating strategy. The approach combines a robust electroless silver coating, a corrosion-inhibiting thiol self-assembled layer, and a protective polymer encapsulation. The optimized composite fabric demonstrates exceptional EMI shielding effectiveness, achieving up to 57.74 dB in the X-band, primarily attributed to a reflection mechanism. A notable achievement of this work is the remarkable breathability of the shielding fabric (2436.1 mm s^{-1}), which

significantly outperforms many conventional materials, highlighting its potential for comfortable wearable applications.

The incorporation of a 1-hexadecanethiol self-assembled film played a critical role in providing outstanding corrosion resistance, as evidenced by a minimal resistance change of only 7.8% after immersion in a Na_2S solution and a corrosion inhibition efficiency of 86.60%. Furthermore, the TPU outer layer served as a mechanical barrier, significantly enhancing the durability and reliability of the conductive network. The composite fabric exhibits excellent operational stability, with negligible changes in electrical resistance after 3000 compression cycles and multiple washing tests, demonstrating superior resistance to mechanical stress and laundering.

This work presents a scalable and viable strategy for designing durable, comfortable, and high-performance EMI shielding textiles. The successful integration of robust shielding, superior breathability, superhydrophobicity, and enhanced durability positions the presented spacer fabric as a promising candidate for advanced applications in next-generation wearable electronics, personal protective equipment, and smart textiles. Future work will focus on further investigating the environmental impact of the fabrication process and exploring the integration of additional smart functionalities, such as physiological sensing, into this versatile platform.

Author contributions

Xiujuan Wang: conceptualization, methodology, investigation, data curation, writing-original draft. Lingzhu Wang: formal analysis, visualization. Yuanjun Liu & Yaming Jiang: methodology, resources. Hao Liu: supervision, funding acquisition, writing-review & editing.

All authors have read and agreed to the published version of the manuscript.

Conflicts of interest

There are no conflicts to declare.

Data availability

The data supporting this article have been included as part of the supplementary information (SI).

Supplementary information is available. See DOI: https://doi.org/10.1039/d5ra09013j.

References

1 X. Yan, F. Guo, Y. Lin, *et al.*, Recent advances in multifunctional electromagnetic interference shielding materials, *Chem. Commun.*, 2025, **61**, 1234.
2 Y. M. Shahandashti, S. Larijani, M. Eskandari, *et al.*, Biomedical potentials of MXene-based self-powered wearable devices: the future of next-generation wearables, *RSC Adv.*, 2025, **15**, 33773.
3 S. M. Sait, S. F. Ahmed and M. R. Rafiq, Experimental study on broadband radiofrequency electromagnetic radiations near cellular base stations: a novel perspective of public health, *J. Therm. Anal. Calorim.*, 2021, **143**, 1935.
4 S. Kumari, J. Dalal, A. Kumar, *et al.*, Enhanced microwave absorption properties of conducting polymer @ graphene composite to counteract electromagnetic radiation pollution: green EMI shielding, *RSC Adv.*, 2024, **14**, 662.
5 H. Gao, Y. Wang and W. Xu, Research Progress of Fiber-Based Electromagnetic Shielding Materials, *Fibers Polym.*, 2025, DOI: 10.1007/s12221-025-00545-0.
6 L. X. Zhao and C. Yang, Research Progress on Electromagnetic Shielding Mechanisms and Textile-Based Protective Materials, *Text. Leather Rev.*, 2024, **7**, 1417.
7 S. Sankaran, K. Deshmukh, M. B. Ahamed, *et al.*, Recent advances in electromagnetic interference shielding properties of metal and carbon filler reinforced flexible polymer composites: a review, *Composites, Part A*, 2018, **114**, 49.
8 M. Wang, X. H. Tang, J. H. Cai, *et al.*, Fabrication, mechanisms and perspectives of conductive polymer composites with multiple interfaces for electromagnetic interference shielding: a review, *Carbon*, 2021, **177**, 377.
9 S. Akram, M. Ashraf, A. Javid, *et al.*, Recent advances in electromagnetic interference (EMI) shielding textiles: A comprehensive review, *Synth. Met.*, 2023, **294**, 117305.
10 D. Wang, S. Hu, D. Kremenakova, *et al.*, Evaluation of the wearing comfort properties for winter used electromagnetic interference shielding sandwich materials, *J. Ind. Text.*, 2023, **53**, 15280837231159869.
11 N. N. Wu, Q. Hu, R. B. Wei, *et al.*, Review on the electromagnetic interference shielding properties of carbon-based materials and their novel composites: recent progress, challenges and prospects, *Carbon*, 2021, **176**, 88.
12 J. F. Gao, J. C. Luo, L. Wang, *et al.*, Flexible, superhydrophobic and highly conductive composite based on non-woven polypropylene fabric for electromagnetic interference shielding, *Chem. Eng. J.*, 2019, **364**, 493.
13 W. Ren, Y. Q. Yang, J. Yang, *et al.*, Multifunctional and corrosion resistant poly(phenylene sulfide)/Ag composites for electromagnetic interference shielding, *Chem. Eng. J.*, 2021, **415**, 128574.
14 T. Wan, Y. Liu, C. X. Zhou, *et al.*, Fabrication, properties, and applications of open-cell aluminum foams: a review, *J. Mater. Sci. Technol.*, 2021, **62**, 11.
15 J. C. Luo, L. Wang, X. W. Huang, *et al.*, Mechanically Durable, Highly Conductive, and Anticorrosive Composite Fabrics with Excellent Self-Cleaning Performance for High-Efficiency Electromagnetic Interference Shielding, *ACS Appl. Mater. Interfaces*, 2019, **11**, 10883.
16 Y. Y. Wang, Z. H. Zhou, C. G. Zhou, *et al.*, Lightweight and Robust Carbon Nanotube/Polyimide Foam for Efficient and Heat-Resistant Electromagnetic Interference Shielding and Microwave Absorption, *ACS Appl. Mater. Interfaces*, 2020, **12**, 8704.
17 L. Y. Liang, P. H. Xu, Y. F. Wang, *et al.*, Flexible polyvinylidene fluoride film with alternating oriented graphene/Ni nanochains for electromagnetic interference

shielding and thermal management, *Chem. Eng. J.*, 2020, **395**, 125138.
18 H. Liu, L. L. Zhu, Y. He, *et al.*, A novel method for fabricating elastic conductive polyurethane filaments by *in situ* reduction of polydopamine and electroless silver plating, *Mater. Des.*, 2017, **113**, 254.
19 L. X. Liu, W. Chen, H. B. Zhang, *et al.*, Flexible and Multifunctional Silk Textiles with Biomimetic Leaf-Like MXene/Silver Nanowire Nanostructures for Electromagnetic Interference Shielding, Humidity Monitoring, and Self-Derived Hydrophobicity, *Adv. Funct. Mater.*, 2019, **29**, 1905197.
20 B. Zhou, M. J. Su, D. Z. Yang, *et al.*, Flexible MXene/Silver Nanowire-Based Transparent Conductive Film with Electromagnetic Interference Shielding and Electro-Photo-Thermal Performance, *ACS Appl. Mater. Interfaces*, 2020, **12**, 40859.
21 W. Wang, W. Y. Li, C. C. Gao, *et al.*, A novel preparation of silver-plated polyacrylonitrile fibers functionalized with antibacterial and electromagnetic shielding properties, *Appl. Surf. Sci.*, 2015, **342**, 120.
22 T. T. Li, Y. T. Wang, H. K. Peng, *et al.*, Lightweight, flexible and superhydrophobic composite nanofiber films inspired by nacre for highly electromagnetic interference shielding, *Composites, Part A*, 2020, **128**, 105685.
23 Y. J. Wan, P. L. Zhu, S. H. Yu, *et al.*, Anticorrosive, Ultralight, and Flexible Carbon-Wrapped Metallic Nanowire Hybrid Sponges for Highly Efficient Electromagnetic Interference Shielding, *Small*, 2018, **14**, 1800530.
24 Y. L. Zhang, X. Guo, W. Wang, *et al.*, Highly Sensitive, Low Hysteretic and Flexible Strain Sensor Based on Ecoflex-AgNWs-MWCNTs Flexible Composite Materials, *IEEE Sens. J.*, 2020, **20**, 14118.
25 J. Ghosh, N. S. Rupanty, T. Noor, *et al.*, Functional coatings for textiles: advancements in flame resistance, antimicrobial defense, and self-cleaning performance, *RSC Adv.*, 2025, **15**, 10984.
26 D. L. Fan, N. X. Li, M. G. Li, *et al.*, Polyurethane/polydopamine/graphene auxetic composite foam with high-efficient and tunable electromagnetic interference shielding performance, *Chem. Eng. J.*, 2022, **427**, 131590.
27 X. S. Zhang, X. F. Wang, Z. W. Lei, *et al.*, Flexible MXene-Decorated Fabric with Interwoven Conductive Networks for Integrated Joule Heating, Electromagnetic Interference Shielding, and Strain Sensing Performances, *ACS Appl. Mater. Interfaces*, 2020, **12**, 14459.
28 S. Zhu, M. Y. Wang, Z. Qiang, *et al.*, Multi-functional and highly conductive textiles with ultra-high durability through 'green' fabrication process, *Chem. Eng. J.*, 2021, **406**, 126793.
29 H. Y. Wu, L. C. Jia, D. X. Yan, *et al.*, Simultaneously improved electromagnetic interference shielding and mechanical performance of segregated carbon nanotube/polypropylene composite *via* solid phase molding, *Compos. Sci. Technol.*, 2018, **156**, 87.
30 R. Islam, Y. Sood, H. Mudila, *et al.*, Microwave absorbing properties of polypyrrole-based 2D nanocomposites, *J. Mater. Chem. A*, 2024, **12**, 31004.
31 K. Kim, M. Jung, S. Jeon, *et al.*, Robust and scalable three-dimensional spacer textile pressure sensor for human motion detection, *Smart Mater. Struct.*, 2019, **28**, 065002.
32 Q. W. Wang, H. B. Zhang, J. Liu, *et al.*, Multifunctional and Water-Resistant MXene-Decorated Polyester Textiles with Outstanding Electromagnetic Interference Shielding and Joule Heating Performances, *Adv. Funct. Mater.*, 2019, **29**, 1806812.
33 L. Meng, Y. Ma, Y. Zou, *et al.*, Lightweight, breathable and self-cleaning polypyrrole-modified multifunctional cotton fabric for flexible electromagnetic interference shielding, *Int. J. Biol. Macromol.*, 2024, **274**, 133347.
34 X. Zhao, P. Zhang, S. Zhang, *et al.*, Breathable, robust, and flexible hierarchical design of multifunctional integrated smart textiles for human health management, *Chem. Eng. J.*, 2025, **507**, 160736.
35 R. Moaref, N. M. Mehdipour and U. Sundararaj, Achieving Outstanding Absorption Performance in Electromagnetic Interference Shielding *via* Improving Impedance Mismatch: Sandwiched PP/$CaCO_3$/Ground Tire Rubber/MWCNT Composites, *ACS Appl. Eng. Mater.*, 2025, **3**, 2811.
36 F. Zhang, H. Long, W. Yang, *et al.*, Gradient structural foam-coated fabric for ultra-low reflection electromagnetic interference shielding, *Composites, Part A*, 2026, **201**, 109414.
37 W. Yang, D. Pan, S. Liu, *et al.*, Multifunctional Wearable Conductive Nanofiber Membrane with Antibacterial and Breathable Ability for Superior Sensing, Electromagnetic Interference Shielding, and Thermal Management, *Adv. Funct. Mater.*, 2025, **35**, 2414811.
38 Z. Wang, D. Xing, R. Yin, *et al.*, Breathable and waterproof conductive cotton fabric pressure sensor with distinguished electrothermal and electromagnetic interference shielding performances, *Appl. Mater. Today*, 2024, **38**, 102256.
39 W. Yang, J. Dong, H. Long, *et al.*, Flexible polyimide-based conductive composite film with confined carbon nanotubes networks for EMI shielding and joule heating, *Adv. Nanocompos.*, 2025, **2**, 322–330.
40 R. H. Wu, L. Y. Ma, A. Patil, *et al.*, All-Textile Electronic Skin Enabled by Highly Elastic Spacer Fabric and Conductive Fibers, *ACS Appl. Mater. Interfaces*, 2019, **11**, 33336.
41 L. F. Gao, C. Li, W. C. Huang, *et al.*, MXene/Polymer Membranes: Synthesis, Properties, and Emerging Applications, *Chem. Mater.*, 2020, **32**, 1703.
42 J. Liu, H. B. Zhang, R. H. Sun, *et al.*, Hydrophobic, Flexible, and Lightweight MXene Foams for High-Performance Electromagnetic-Interference Shielding, *Adv. Mater.*, 2017, **29**, 1702367.
43 J. Peng, B. L. Chen, Z. C. Wang, *et al.*, Surface coordination layer passivates oxidation of copper, *Nature*, 2020, **586**, 390.
44 M. F. Li, J. X. Chen, W. B. Zhong, *et al.*, Large-Area, Wearable, Self-Powered Pressure-Temperature Sensor Based on 3D Thermoelectric Spacer Fabric, *ACS Sens.*, 2020, **5**, 2545.

45 Y. T. Wang, H. K. Peng, T. T. Li, *et al.*, MXene-coated conductive composite film with ultrathin, flexible, self-cleaning for high-performance electromagnetic interference shielding, *Chem. Eng. J.*, 2021, **412**, 128676.
46 X. H. Zheng, W. Q. Nie, Q. L. Hu, *et al.*, Multifunctional RGO/Ti_3C_2Tx MXene fabrics for electrochemical energy storage, electromagnetic interference shielding, electrothermal and human motion detection, *Mater. Des.*, 2021, **200**, 10.
47 R. Cao, X. J. Pu, X. Y. Du, *et al.*, Screen-Printed Washable Electronic Textiles as Self-Powered Touch/Gesture Tribo-Sensors for Intelligent Human-Machine Interaction, *ACS Nano*, 2018, **12**(6), 5190–5196.